*International Journal of Microwave and Wireless Technologies*

**cambridge.org/mrf**

# Dual-polarized unit cell for liquid crystal reconfigurable intelligent surface based on defected delay lines

Robin Neuder[1], Ana Díaz-Rubio[2], Yingzhe Liu[1], Nora Dzieia[1], Dongwei Wang[1] and Alejandro Jiménez-Sáez[1]

[1]Institute of Microwave Engineering and Photonics, Technische Universität Darmstadt, Darmstadt, Germany and [2]Nanophotonics Technology Center, Universitat Politècnica de València, València, Spain

**Research Paper**

**Cite this article:** Neuder R, Díaz-Rubio A, Liu Y, Dzieia N, Wang D, Jiménez-Sáez A (2025) Dual-polarized unit cell for liquid crystal reconfigurable intelligent surface based on defected delay lines. *International Journal of Microwave and Wireless Technologies* **17**(9), 1533–1541. https://doi.org/10.1017/S1759078725102596

Received: 31 January 2025
Revised: 10 October 2025
Accepted: 17 October 2025

**Keywords:**
Defected ground structure; Liquid crystal; Reconfigurable intelligent surface; Reflectarray; Unit cell

**Corresponding author:** Robin Neuder; Email: robin.neuder@tu-darmstadt.de

**Abstract**

This paper presents the design and characterization of a unit cell for dual-polarized liquid crystal (LC)-based reconfigurable intelligent surfaces (RIS), as well as an efficient, full-wave simulation methodology for the far-field beam-steering capabilities of large-scale LC-RIS. Within this framework, the unit cell relies on defected delay lines with a 4.6 $\mu$m thin LC layer aperture coupled to a patch antenna. This delay line architecture aims towards simultaneous optimization of loss, bandwidth and response time. Full-wave simulations of the unit cell in a periodic environment show an operating frequency between 26.5 and 29.5 *GHz* with wide angle radiation. Measurements of the unit cell in a $3 \times 3$ rectangular grid exhibit wideband impedance matching and overall good agreement with simulations. Furthermore, a simulation methodology is introduced that evaluates large-scale LC-RIS far-field beam-steering capabilities without requiring full-wave simulations of the entire structure, but just few unit cells. Within this scope, the LC-RIS achieves a maximum efficiency of 20.8% with a beam-steering range from −48° to +48°, despite the use of a lossy glass substrate and gold as a conductor. It exhibits a minimum bandwidth of 8.2% for an efficiency of at least 10% across all analyzed steering angles in E-Plane and H-Plane.

## Introduction

The emergence of reconfigurable intelligent surfaces (RISs) has sparked widespread interest due to their promise in advancing wireless millimeter wave and terahertz systems. As passive, tunable reflectors, RISs present an economically viable solution for overcoming hurdles in establishing robust communication links [1, 2]. From a hardware standpoint, a RIS can be conceptualized as a tunable reflectarray without a predefined feed. It comprises a periodic arrangement of individually tunable unit cells capable of adaptively manipulating electromagnetic waves. This manipulation enables arbitrary bending and rotation of wavefronts, facilitating either near-field focusing or far-field directing towards end users. An exemplary outdoor scenario is depicted in Fig. 1. Depending on the envisioned use case, there are several requirements a RIS should fulfill including low loss, wide bandwidth, wide angle beam-steering capabilities, fast response time, low power consumption and low cost.

In order to implement a RIS, a radiating element as well as a phase shifting mechanism are required. Conventionally, the phase shifting mechanism is realized with positive intrinsic negative (PIN) or varactor diodes. Promising realizations have been presented in [3] and [4]. However, at least one diode is required for each unit cell. As a result, power consumption and cost become serious challenges in large scale RIS, particularly since the cost for diodes tends to increase with frequency. These challenges are particularly pronounced considering the findings in [5], i.e.: at least hundreds of unit cells are required for a RIS to outperform active relay stations.

A promising alternative for the phase shifting mechanism are nematic LCs. By making use of the anisotropic nature of the LC molecules, tunable resonators and delay lines can be realized. There exist several challenges with LC, i.e. moderate insertion loss, temperature sensitivity and comparably slow response times compared to competing technologies such as semiconductors or MEMS [6]. Nonetheless, LC also provides several benefits such as continuous tunability and applicability from the low GHz range up to several THz due to its decreasing loss with frequency. However, the most meaningful advantages come into play when LC is considered for large, flat surfaces: Its intrinsically low power consumption and low cost [7].

There exist two architectures to realize flat tunable LC surfaces: The resonant architecture (RA) and the delay line architecture (DLA). The RA relies on the detuning of a resonant radiating element such that radiating and phase shifting layer are combined [8]. Its advantage is its simplicity, but it lacks the possibility to optimize towards wide bandwidth,

© The Author(s), 2025. Published by Cambridge University Press in association with The European Microwave Association. This is an Open Access article, distributed under the terms of the Creative Commons Attribution licence (http://creativecommons.org/licenses/by/4.0), which permits unrestricted re-use, distribution and reproduction, provided the original article is properly cited.

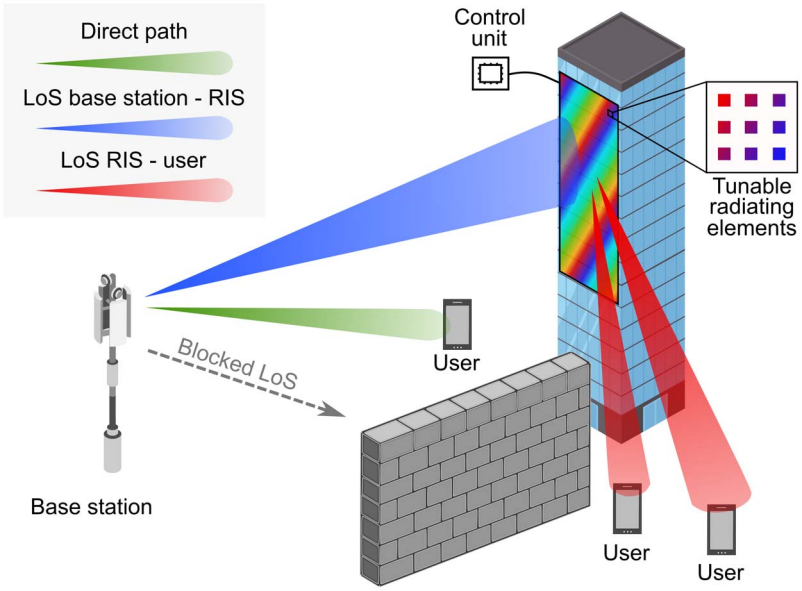



**Figure 1.** Exemplary outdoor scenario for a RIS. The different colors in the RIS qualitatively indicate different reflected phase at the radiating elements. LoS: Line-of-sight.

low loss and fast response time simultaneously [9]. In the DLA, radiating layer and phase shifting layer are separated. By making use of a tunable delay line coupled to a radiating element, LC-RIS can be optimized towards bandwidth, loss and response time simultaneously. The functionality of this approach for LC-RIS has been demonstrated for a single linearly polarized RIS with 120 elements at 60 GHz [9].

In light of the above, the DLA is considered in this contribution. In order to prove its feasibility in a dual linear polarized RIS, a unit cell is designed, fabricated and characterized around a center frequency of 28 GHz. This paper is structured as follows: First, the dual-polarized LC-RIS design is introduced and simulation results in a periodic environment are presented. Subsequently, the characterization results of a fabricated sample are shown. In addition, a comprehensive evaluation method for large-scale LC-RIS is introduced, enabling the analysis of beam-steering capabilities by simulating only a few unit cells. Finally, a conclusion is given. An earlier version of this paper was presented at EuMW 2024 and was published in its Proceedings [10].

## Unit cell design

The layout of the dual-polarized LC-RIS based on the DLA is illustrated in Fig. 2a. Here, the unit cells are arranged in a rectangular grid. Each radiating element is coupled to two distinct tunable delay lines, one for each linear polarization. As shown in the side view, the incoming electromagnetic wave is coupled from the radiating element to the tunable delay line via aperture coupling. As a result, the wave travels through the delay line, is reflected at an open end and travels back to the radiating element, from which it is re-radiated. It is important to note that the element spacing should remain $\leq 0.5\,\lambda_0$ to avoid grating lobes in the visible plane. Furthermore, complete 360° phase tunability must be ensured in every delay line to fully exploit the continuous phase tunability of LC-based delay lines. Hence, the delay line topology must provide significant tunability in a limited space. In other words, a high compactness of the tunable delay line is required. Additionally, the delay line topology should also provide fast response time, low loss and wide bandwidth. For a fast response time in the order of milliseconds, a thin LC layer thickness $t_{\mathrm{LC}}$ of few µm is required [7].

As conventional topologies such as microstrip lines or coplanar waveguides lack compactness and lead to increasing conductor losses with decreasing substrate thickness [11], special delay line topologies must be employed. For that purpose, the defected ground structure inverted microstrip line (DGS-IMSL) is proposed as a tunable delay line for LC-RIS in [11] and [12]. It is based on periodic defects in the ground plane of an inverted microstrip line (IMSL) resulting in a periodical loading of a series of capacitors. On top of reducing conductor losses (and hence, enabling thin $t_{\mathrm{LC}}$), this topology increases compactness, making it a promising candidate for the use in DLA-based LC-RIS.

The materials used in this study are 700 $\mu$m thick AF32 glass from Schott ($\varepsilon_r = 5.1$ and $tan\delta = 0.009$ at 24 GHz [13]), GT7-29001 ($\varepsilon_{r,\perp} = 2.45$, $\varepsilon_{r,|} = 3.53$, $tan\,\delta_\perp = 0.0116$ and $tan\delta_| = 0.0064$ at 19 GHz [14]) from Merck as the tunable LC mixture and gold as a conductor. The LC thickness $t_{\mathrm{LC}}$ corresponds to 4.6 $\mu$m. With these materials, the DGS-IMSL provides a figure of merit (FoM) of 75°/dB and a normalized length of $0.4\,\lambda_0$ at 27.5 GHz as demonstrated in [11]. In other words, for full 360° tunability, the DGS-IMSL introduces a loss of 4.8 dB and requires a length of $0.4\lambda_0$. Due to the additional space required for the radiating element, this compactness does still not suffice for an element spacing of $0.5\lambda_0$. Hence, as visible in the sketch of the unit cell in Fig.2a, the defected delay line is bent and the element spacing is increased to $0.536\lambda_0$, which still enables grating lobe free steering between −60° and +60°. Simulations show that the applied bending of the DGS-IMSL does not deteriorate its performance.

Electromagnetic simulations have been performed with CST Studio Suite 2024. Here, the unit cell is evaluated in a periodic environment, so that mutual coupling is taken into account. The impedance matching of the unit cell is exemplified in Fig. 2b for both extreme LC orientations achievable with the given topology ($\varepsilon_{r,LC} = 2.6$ and $\varepsilon_{r,LC} = 3.53$ – for details, see [11]) and an intermediate state. It shows good matching behavior below −10dB for all LC states over the whole desired frequency range. Note that

https://doi.org/10.1017/S1759078725102596 Published online by Cambridge University Press

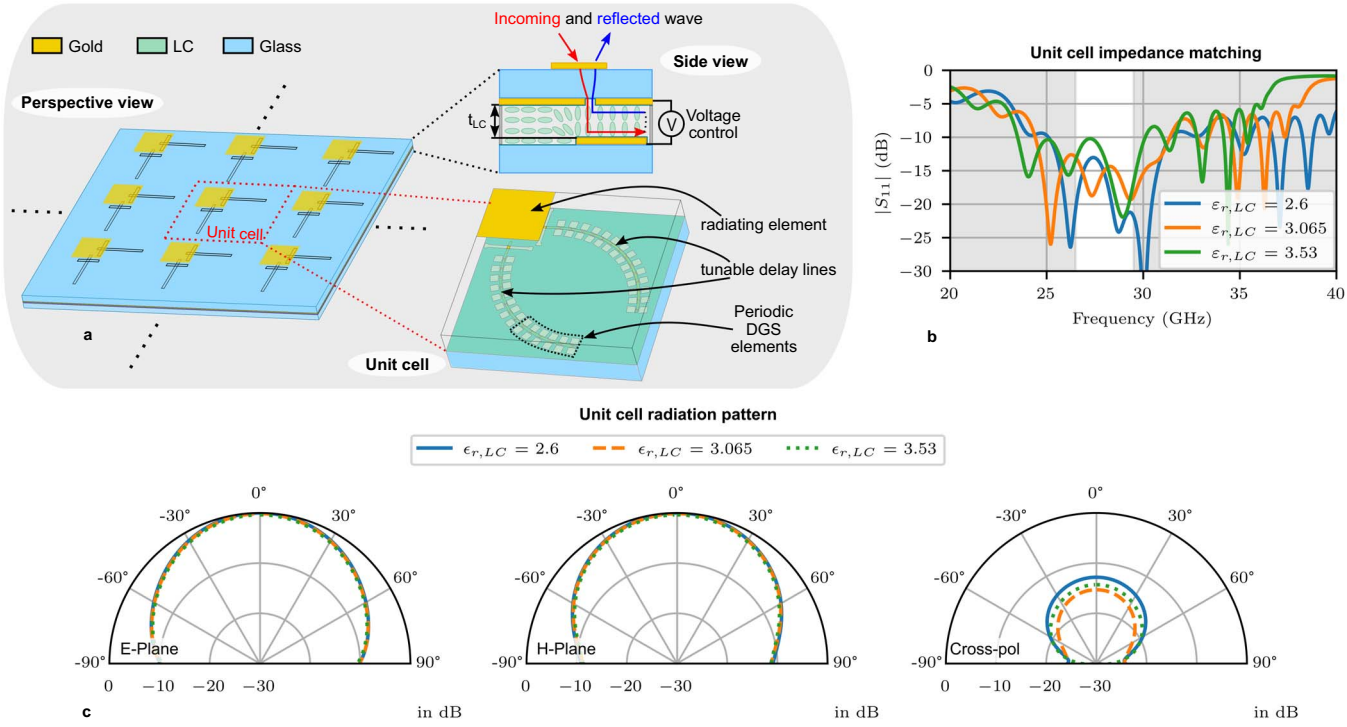



**Figure 2.** Unit cell characterization in simulations. (a) The perspective view of a 3 × 3 cut-out of a RIS and the side view of a tunable LC delay line coupled to a radiating element as well as the proposed dual-polarized LC-RIS unit cell. (b) The impedance matching of a unit cell, while (c)–(e) display its normalized radiation patterns.

all presented results are valid for both linear polarizations as the setup is symmetric. The normalized radiation patterns are exemplified in Fig. 2c. The unit cell shows wide angle radiation in both planes and a cross polarization below −12dB. Additionally, it is worth noting that the proposed dual-polarized unit cell exhibits scalability towards at least few hundreds of GHz.

Due to the limited space in the unit cells, the biasing scheme must also be addressed. In a fully assembled LC-RIS, two-dimensional beam steering can be realized using thin-film transistors. This approach, already established in liquid crystal displays (LCDs), enables element-wise biasing within a matrix and requires only N bias lines for the rows and M bias lines for the columns (see [9],[15]).

## Unit cell measurement

In the previous section, simulation results for the proposed unit cell performance in a periodic environment are presented. In order to prove the performance in measurements, the unit cell is characterized as the center element in a 3 × 3 rectangular grid as presented in Fig. 3a. This modified setup provides an approximation of the periodic unit cell environment as the central element experiences mutual coupling from all its surrounding elements. The sample was fabricated using standard lithographic processes [16]. The exact dimensions of an unit cell are provided in the Supplementary Material Fig. 7. In order to enable coupling to a coaxial connector, the length of the DGS-IMSL delay line of the central unit cell is extended towards the boundaries of the 3x3 rectangular setup. For the sake of simplicity, the sample is characterized in the unbiased state only ($\varepsilon_{r,LC} = 2.6$). The antenna performance is measured with a Keysight VNA PNA-X N5247A and a standard 16 dBi gain horn antenna at a distance of approximately 60 cm.

The measured impedance matching of the unit cell is presented in Fig. 3b. Good matching is achieved in the desired frequency range between 26.5 and 29.5 GHz in good agreement with the simulations. The measured response times of a tunable delay line with GT7 and $t_{LC} = 4.6\,\mu$m correspond to 72 and 15 ms, for the switch-off and switch-on response times, respectively. On that basis, Delbari et al. [17] shows that beam re-allocation in a large LC-RIS can be completed within less than 10 ms, depending on the considerations.

The extended defected delay line induces significant loss such that small parasitic influences (i.e. fabrication tolerances and the coaxial connector) have a deteriorating impact on the radiation pattern. In order to reduce parasitic influences, a time gating has been applied for evaluation of the radiation patterns to isolate the response of the antenna from undesired interfering signals.

Measured radiation patterns of the fabricated samples are presented in Fig. 3c. E- and H-plane show results comparable to simulations of the modified sample for all frequencies. Particularly the results for the E-plane reveal noticeable deterioration when compared to unit cell simulations in a periodic environment, mainly due to the extended delay line and the presence of the coaxial connector in that plane. Measured and simulated cross polarization is increased compared to unit cell simulations. However, measured values at 28 GHz match with simulations of the modified setup and peak at around −8.5 dB at this frequency.

## Far-field beam-steering capabilities

In addition to the aforementioned unit cell features, the far-field beam-steering capabilities of the dual-polarized unit cell can be evaluated in terms of efficiency, loss contributions and bandwidth. However, a simulation of a large RIS with hundreds or even

https://doi.org/10.1017/S1759078725102596 Published online by Cambridge University Press

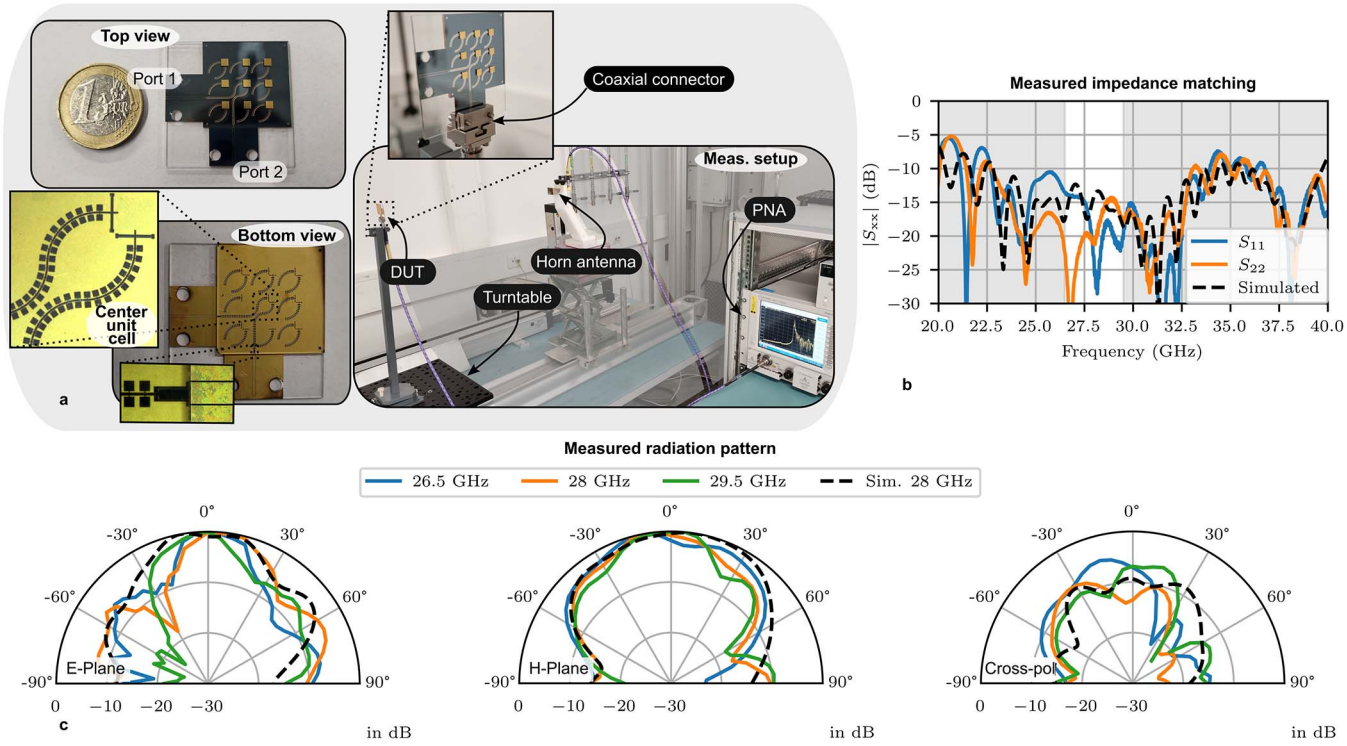



**Figure 3.** Unit cell characterization in measurements. (a) The fabricated sample from top and bottom view as well as the measurement setup. (b and c) The measured impedance matching at port 1 and port 2 and the radiation pattern of the sample, respectively.

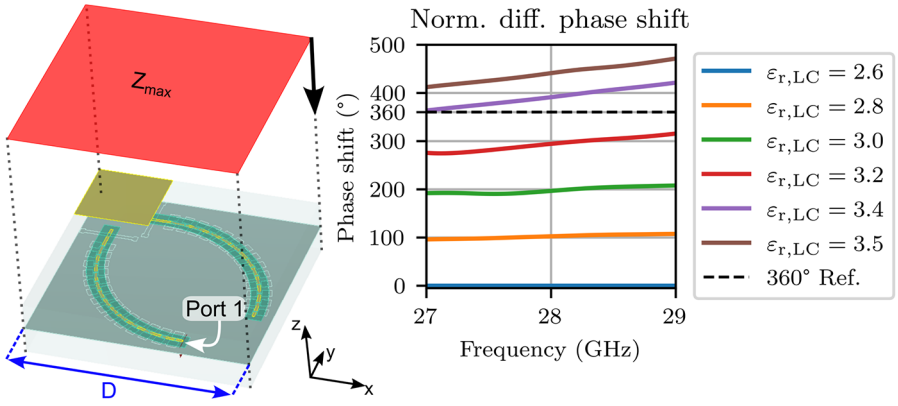



**Figure 4.** Evaluation of unit cell phase shift with regard to the applied liquid crystal permittivity. On the left, the simulation setup is shown. $Z_{\max}$ and Port 1 are the two simulation ports for excitation and reception of the electromagnetic modes. The black arrow attached to the $Z_{\max}$ port indicates its orientation.

thousands of elements is a tedious process. This is particularly relevant for the DLA approach with thin $t_{LC}$, as the phase shifter requires fine meshing, leading to high computational demands. Instead, we propose a simulation methodology to characterize the LC-RIS far-field beam-steering capabilities that significantly reduces computational complexity by requiring simulations of only a few unit cells instead of the entire structure.

First, the differential phase shift range inside the unit cell must be evaluated. The normalized differential phase shift and its dependence on the LC permittivity are presented in Fig. 4. The simulation setup consists of a square unit cell, with period $D$, and two ports. The first port, Port 1, is applied directly to the phase shifter, and the second port is located on top of the simulation volume, at $Z_{\max}$, and excites/receives plane wave modes. To analyze the phase shift, a wave is excited at Port 1 and received at the plane wave port $Z_{\max}$. The simulated phase shifts are compared across the permittivity range of the applied LC-mixture. They are normalized to the lowest phase shift, corresponding to a permittivity of $\varepsilon_{r,LC} = 2.6$. Furthermore, the phase shifts are doubled because, in the desired LC-RIS operating in reflection mode, the wave passes through the unit cell twice. At 28 GHz, the results show that less than $\varepsilon_{r,LC} = 3.4$ is required for full 360° tunability. Thus, the unit cell design accounts for a potential 20% reduction in the total differential phase shift, which may result from the tolerances of the device fabrication. Hence, if fabrication tolerances are negligible, the phase shifter could be shortened to minimize losses.

With the knowledge of the permittivity-phase shift mapping, the beam steering capabilities can be analyzed. The focus lies on the evaluation of the co-polarization efficiencies and the determination of the sources of loss. The latter can be subdivided into material losses and mode conversion, e.g. cross-polarization or steering to undesired angles. To this end, there exist two approaches to

https://doi.org/10.1017/S1759078725102596 Published online by Cambridge University Press

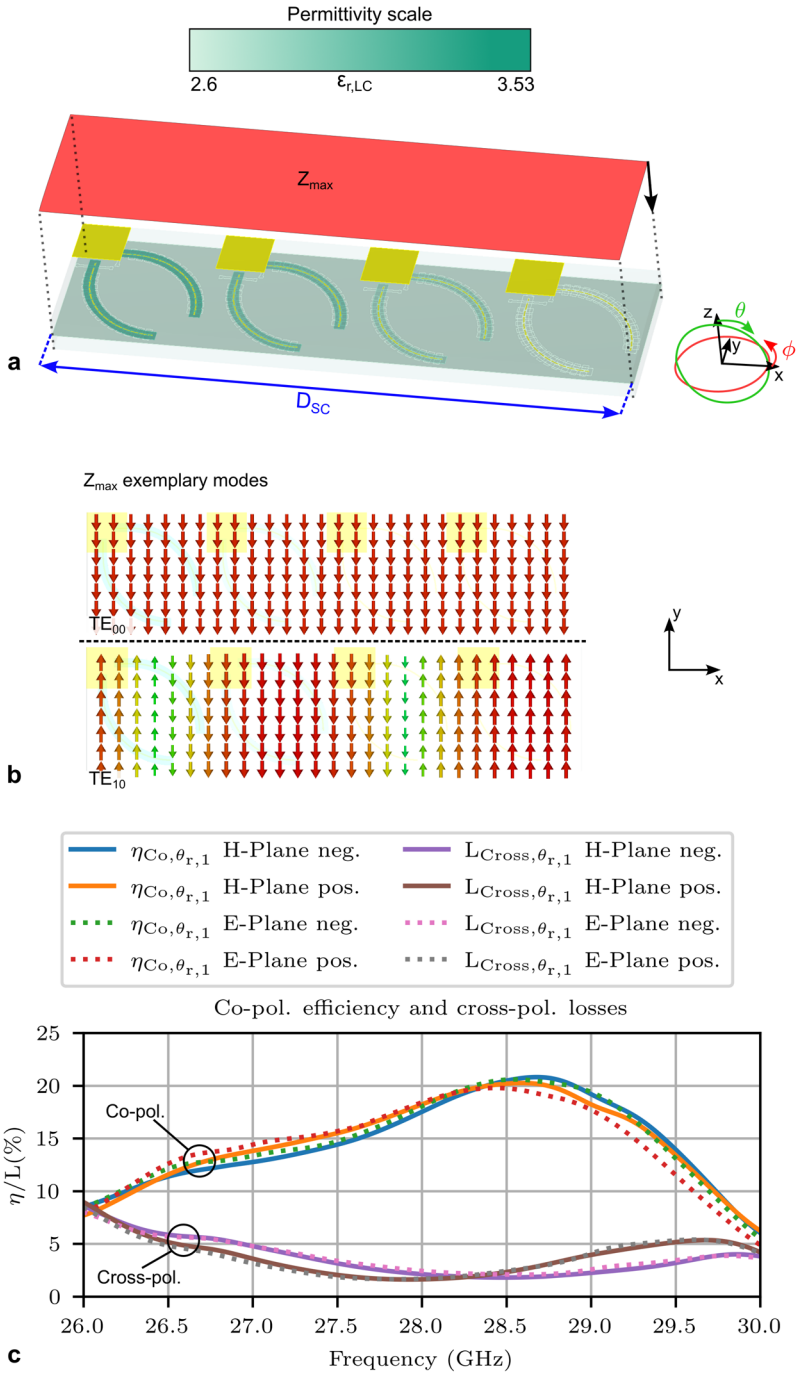



**Figure 5.** Efficiency calculation of the infinite size metasurface using Floquet-mode theory. (a) Representation of the simulation setup. (b) Exemplary excitation modes for the provided example corresponding to the specular mode and the first diffracted mode. (c) Co-polarization efficiency and cross-polarization losses for the 4 element unit cell steering towards the first diffracted mode. The acronyms neg. and pos. correspond to a steering towards the negative $\theta$ and the positive $\theta$ direction, respectively, corresponding to $\theta_{r,1} = \pm 28^{\circ}$ at 28 GHz.

evaluate beam steering capabilities in terms of efficiencies and losses with this numerical setup:

- **Approach 1:** Floquet mode-scattering analysis that takes into account an infinite metasurface made of supercells with $N$ unit cells and calculates the scattering into a discrete number of plane waves.
- **Approach 2:** Far-field efficiency analysis that considers a limited number of periodic supercells, $M$, composed by $N$ unit cells.

Using Approach 1, the periodicity of the metasurface will be defined by the number of unit cells $N$ in the metasurface, leading to a supercell with $D_{sc} = ND$ (see Fig. 5a). $D_{sc}$ is the periodicity of the supercell composed by $N$ unit cells.

For an infinite periodic structure illuminated by a plane wave, the tangential wavenumber of the diffracted modes is given by the Floquet condition:

$$k_{x,n} = k \sin\theta_i + \frac{2\pi n}{D_{sc}}, \tag{1}$$

where $k$ is the wavenumber at the operation frequency, $k_{x,n}$ is the tangential component of the wave vector of each Floquet mode, $\theta_i$ is the incidence angle and $n$ denotes the order of the Floquet mode. Here, $n = 0$ corresponds to specular reflection. Following

https://doi.org/10.1017/S1759078725102596 Published online by Cambridge University Press

this definition, the normal component of the wave vector is given by $k_{y,n} = \sqrt{k^2 - k_{x,n}^2}$, and only the modes with $k > k_{x,n}$ propagate into free space. For a propagating mode, the reflection angle is determined by:

$$\theta_{r,n} = \arctan\left(\frac{k_{x,n}}{k_{y,n}}\right). \tag{2}$$

The incident power is distributed among these propagating modes depending on the configuration of the $N$ unit cells that compose the supercell.

In our numerical model, the incoming wave is excited at $Z_{\max}$ emulating a plane wave impinging from broadside the simulation domain, exemplified by the $TE_{00}$ mode (see Fig. 5b) for representation of fields at the port for normal incidence. The energy reflected into specular direction, $\theta_{r,0} = \theta_i$ will share the same profile. Cross-polarization in specular direction can also be characterized, such as through conversion into modes like $TM_{00}$. In our case, the energy send towards the desired direction, $\theta_{r,1}$, is modeled by the coupling of energy into $TE_{10}$ mode and the cross-polarization in this direction by the coupling of energy into $TM_{10}$.

In the given example with four single element unit cells, $D_{SC} = 4\,N$, each element has an inter-element differential phase shift of 90°. Hence, the phases assigned to the elements are 0°, 90°, 180°, 270°, respectively. Notice that these phases are inserted in the simulation as LC substrates of varying permittivities. With regard to the inter-element spacing of $0.536\lambda_0$, a 90° inter-element phase shift accords to a steering towards approximately $\theta_{r,1} = 28°$ at 28 GHz. Fig. 5c illustrates the broadband far-field co-polarization efficiency and cross-polarized scattering, with steering towards $\theta_{r,1} = -28°$ in the E-Plane and H-Plane as the phase gradient is oriented towards negative $x$.

With the proposed setup, a range of reflected angles $\theta_r$ have been evaluated. For that purpose, supercells with sizes of $D_{SC} = 6\,N$, $D_{SC} = 4\,N$ and $D_{SC} = 3\,N$ were considered, enabling the analysis of inter-element phase shifts of 60°, 90°, 120°, respectively. Notice that the angle of reflection changes with number of elements according to Eq. 2.

However, this approach inherently limits the evaluation to a discrete set of reflection angles $\theta_r$. To relax this limitation, we extend the analysis with an additional non-integer supercell size of $D_{SC} = 2.5\,N$ corresponding to an inter-element phase shift of 144°. This approach can also be modeled as a supercell with $D_{SC} = 5\,N$ analyzing the second-order Floquet mode ($n = 2$) instead of the first mode ($n = 1$).

The calculated reflected angles $\theta_{r,n}$ are summarized in Table. 1. The applied permittivities to realize the desired phase shifts are provided in the Supplementary Material Table 1. Fig. 5c displays the co-polarization efficiencies $\eta_{Co}, \theta_{r,1}$ and the cross-polarization losses $L_{Cross}, \theta_{r,1}$ for $D_{SC} = 4\,N$. The outcomes for $D_{SC} = 6\,N$, $D_{SC} = 5\,N$ and $D_{SC} = 3\,N$ are provided in the Supplementary Materials Figs. 5 and 6.

The second approach to evaluate efficiency, Approach 2, goes one step further and considers the effect of a finite number of supercells in the RIS [18, 19]. The goal of our study will be to consider that the RIS is made by an arrangement of $M \times NM$ supercells in $xy$-plane. In Fig. 6a, the simulated electric far-field pattern of a single element unit cell is depicted at 28 GHz. It is important to notice that in this simulation, due to the small periodicity of the unit cell, we do not operate on the metagrating regime where Floquet modes can propagate [20] and it is not expected to have beam steering. By expanding the single element unit cell to the $N = 4$ element supercell configuration with different permittivities, the far-field distribution becomes more focused and is steered towards the $-\theta$ direction, as it is shown in Fig. 6b. Finally, the four element supercell from (b) is scaled to a large LC-RIS with $M = 9$ supercells (1296 elements). In other words, the unit cell element factor obtained in (b) is multiplied with the array factor in (c), which enables the evaluation of the far-field beam-steering capabilities of a large LC-RIS to be simulated by modeling only a small section instead of the entire structure.

In Fig. 6d and g, the broadband co-polarization efficiencies $\eta_{Co}$ of the presented setup are displayed in heat maps for E- and H-plane. These efficiencies are calculated as the ratio of the radiated electric far-field in the outgoing direction and the maximum reflected electric far-field of a perfectly conducting metal plate with the same size and distance to the plane wave port:

$$\eta_{Co} = \frac{\mathrm{Mag}_{Co,RIS}(\theta_r, \phi_r)}{\mathrm{Mag}_{MP,max}\,\cos(\theta_i)\,\cos(\theta_r)}. \tag{3}$$

$\mathrm{Mag}_{RIS}(\theta_r, \phi_r)$ refers to the co-polarized electric far-field magnitude of the LC-RIS depending on the direction of the reflection of the wave described by $\theta_r$ and $\phi_r$. $\mathrm{Mag}_{MP,max}$ refers to the maximum received electric far-field magnitude of the metal plate. The cosine terms account for the magnitude reduction regarding the angle of the incident and reflected waves, $\theta_i$ and $\theta_r$, respectively. Since all simulations are performed for an incident wave from broadside, Eq. 3 simplifies to:

$$\eta_{Co} = \frac{\mathrm{Mag}_{Co,RIS}(\theta_r, \phi_r)}{\mathrm{Mag}_{MP,max}\,\cos(\theta_r)}. \tag{4}$$

The heatmaps show that the steering works equally well in E- and H-plane. Around its operating frequency, the LC-RIS starts to act like a metal plate, reflecting the wave back to broadside. The visible inclination of the steered beam arises from beamsquinting effects, which become more severe for larger steering angles.

Fig. 6e and h depicts the co-polarization efficiencies obtained from full-wave simulations for various supercell sizes $D_{SC}$ at 28 GHz in E- and H-plane. The full-wave results exhibit excellent agreement with the theoretically obtained values for the reflected angle $\theta_{r,n}$ listed in Table 1. Furthermore, it is shown that the LC-RIS supports wide angle beam-steering with only a fraction of the efficiency being lost. In Fig. 6f and i, the cross-polarization is given at 28 GHz in E- and H-plane. Cross-polarization losses can be computed using Eq. 4 by replacing $\mathrm{Mag}_{Co,RIS}(\theta_r, \phi_r)$ with $\mathrm{Mag}_{Cross,RIS}(\theta_r, \phi_r)$, the cross-polarized electric far-field magnitude. In addition to the presented plots, the heat maps for co-polarization efficiency and cross-polarization loss for all examined steering angles in both planes can be found in the Supplementary Material Figs. 1–4.

When comparing the two efficiency/loss evaluation approaches, each offers distinct advantages and disadvantages. Approach 2 provides detailed information on the exact steering angles for all evaluated frequency points considering a finite-size RIS. However, it requires numerous far-field computations (at each desired frequency point) and an additional post-processing step to compare results with a metal plate. Approach 1 eliminates the need for post-processing and directly delivers broadband results with precise values for all mode conversions considering an infinitely sized RIS. Its limitation, however, lies in the inability to generate a radiation diagram. In summary, both approaches yield identical results for efficiencies and losses. Depending on the required information,

https://doi.org/10.1017/S1759078725102596 Published online by Cambridge University Press

**Table 1.** Calculation of reflection angles $\theta_{r,n}$ for different supercell sizes at 28 GHz

| $D_{SC}$ | Phase shift | $k_{x,n}$ (1/m) | $k_{y,n}$ (1/m) | $\theta_{r,n}$[a] |
|---|---|---|---|---|
| $6\,N$ | 60° | $k_{x,1} = 182.4$ | $k_{y,1} = 557.6$ | $\theta_{r,1} = 18.1°$ |
| $4\,N$ | 90° | $k_{x,1} = 273.5$ | $k_{y,1} = 519.1$ | $\theta_{r,1} = 27.8°$ |
| $3\,N$ | 120° | $k_{x,1} = 364.7$ | $k_{y,1} = 459.6$ | $\theta_{r,1} = 38.4°$ |
| $2.5\,N$[b] | 144° | $k_{x,1} = 437.6$ | $k_{y,1} = 390.8$ | $\theta_{r,1} = 48.2°$ |
| $5\,N$ | 144° | $k_{x,2} = 437.6$ | $k_{y,2} = 390.8$ | $\theta_{r,2} = 48.2°$ |

[a]Calculated with Eq. 2.
[b]Equals $D_{SC} = 5\,N$ for the second Floquet mode order $n = 2$.

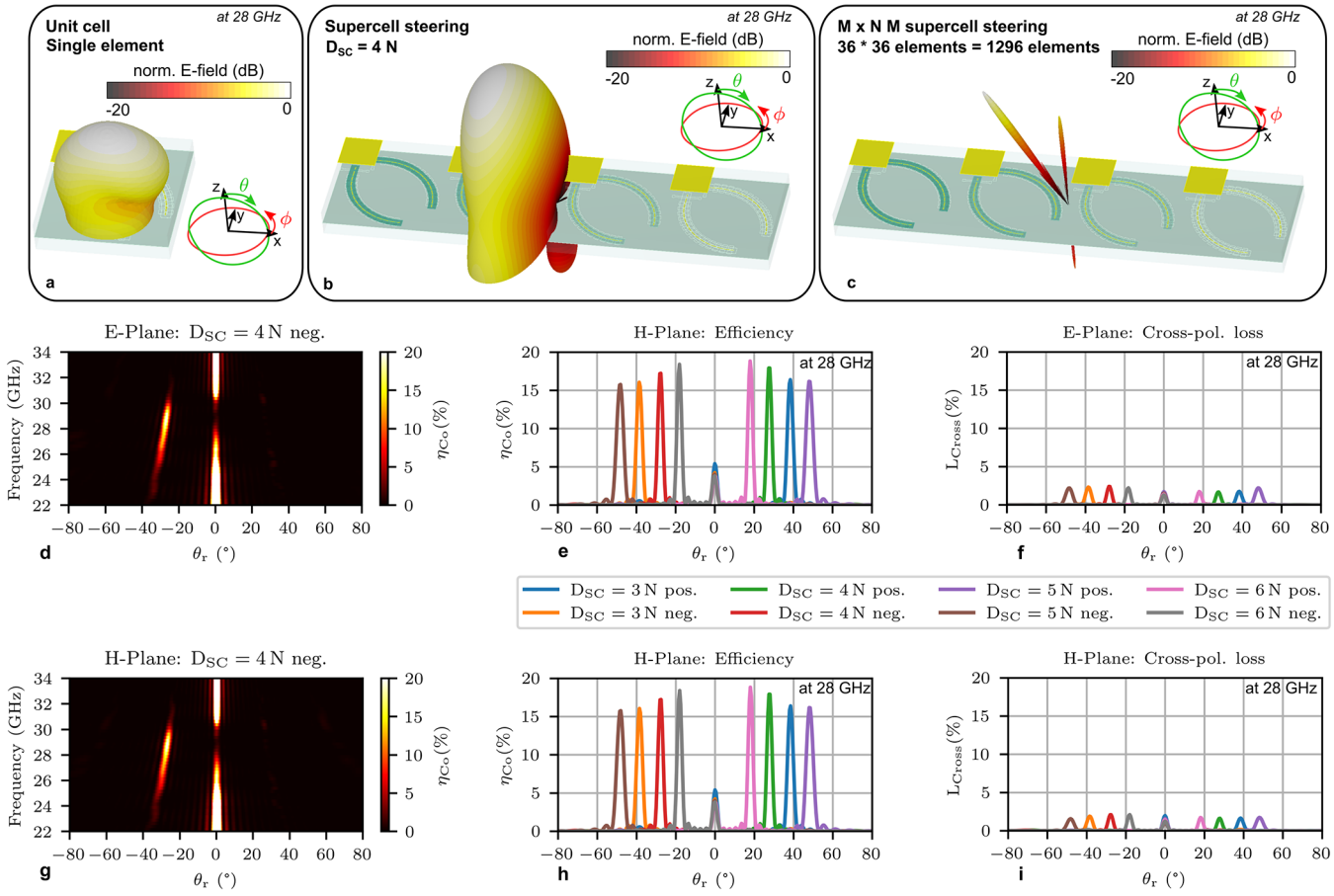



**Figure 6.** Efficiency calculation for a finite size reconfigurable intelligent surface composed of the proposed dual-polarized liquid crystal-based unit cell. (a) The radiated far-field pattern of an unit cell with one element. (b) The radiated far-field pattern of a $D_{SC} = 4\,N$ supercell with an inter-element phase shift of 90°. (c) The radiated far-field pattern of 1296 ($36 \times 36$) elements, accomplished by multiplication of (b) with the array factor. The red-yellow-white (hot) color grading marks the intensity of the radiated electric field. The green color grading indicates the applied liquid crystal permittivity. Note: In the setup, the ground plane has been hidden to make the liquid crystal layer visible. (d and g) The broadband performance in terms of the steering efficiency in a heat map for the E-plane and the H-plane, respectively. (e and h) as well as (f and i) The results of the co-polarization efficiency $\eta_{Co}$ and the cross-polarization loss $L_{Cross}$ for the E-plane and the H-plane.

one approach may offer advantages over the other. However, since both can be derived from the same simulation file, a combination of the two is often recommended.

To conclude this paper, an analysis of the maximum efficiency of the dual-polarized LC-RIS unit cell is presented, along with a breakdown of the loss contributions. The results are obtained from the $D_{SC} = 4\,N$ supercell. The maximum co-polarized steering efficiency of the LC-RIS reaches 20.8% at 28.65 GHz. The total losses of 79.2% are composed of material losses and power converted to undesired modes. The material losses account for 71.7%, divided in 41.1% dielectric losses (caused by the non-zero *tanδ* of the LC-mixture and glass substrate) and 30.6% conductor losses (caused by the finite conductivity of gold). Mode conversion accounts for a total of 7.5%. 1.9% and 1.3% are lost due to cross-polarization towards the steering angle $\theta_{r,1}$ and broadside, respectively. Cross-polarization could be further mitigated by applying careful consideration to the design and positioning of the coupling slot (e.g. see [21]), ensuring that its geometry does not introduce unwanted field asymmetries. In addition to cross-polarization loss, 1.8% of the power are radiated towards

https://doi.org/10.1017/S1759078725102596 Published online by Cambridge University Press

**Table 2.** Summary of dual-polarized LC-RIS unit cell performance

| Frequency (GHz) | Bandwidth[a] (%) | Max. Co-pol. efficiency[b] (%) | Cross-pol. loss[b] (%) | Material loss[bc] (%) | Steering range | LC thickness (μm) | Response time (ms) |
|---|---|---|---|---|---|---|---|
| 26.4–28.65 | 8.2 | 20.8 | 1.9 | 71.7 | $-48^\circ$ to $+48^\circ$ | 4.6 | 15 ($\tau_{on}$) - 72 ($\tau_{off}$) |

[a]The minimum bandwidth required for efficiencies greater than 10% for all analyzed steering angles in both the E- and H-plane is evaluated, as shown in the supplementary material Fig. 5.
[b]Evaluated for steering towards $\theta_{r,1} = -28^\circ$ ($D_{SC} = 4\,N$) at 28.65 GHz.
[c]Dielectric (glass substrate and liquid crystal) and conductor (gold) losses.

the opposite side of the LC-RIS and 1.1% are reflected back to broadside. The remaining 1.4% are converted to various other undesired modes.

Thus, the unit cell loss is mainly determined by the lossy materials and could be considerably reduced with lower loss materials (for details, see [9]). In Table 2, the features of the proposed LC-RIS are summarized.

## Conclusion

This paper presents the design and comprehensive characterization of a unit cell for a dual-polarized liquid crystal reconfigurable intelligent surface operating at approximately 28 GHz. The unit cell is based on defected delay lines with a thin 4.6 $\mu$m liquid crystal substrate and aims for optimization of bandwidth, loss and response time simultaneously. Within this scope, measurements of the unit cell show good agreement with simulations in terms of impedance matching and single-element radiation characteristics. Additionally, a method is introduced to analyze the far-field beam-steering capabilities of a large-scale liquid crystal reconfigurable intelligent surface, requiring simulations of only a few unit cells rather than the entire surface. The results show a 10% efficiency bandwidth of 8.2% in a steering range from $-48^\circ$ to $+48^\circ$ in both, the E-Plane and the H-Plane. A maximum efficiency of 20.8% is accomplished.

**Acknowledgements.** This work was funded by the Deutsche Forschungsgemeinschaft (DFG, German Research Foundation) – Project-ID 287022738 – TRR 196 MARIE within project C09. In addition, thanks goes to Merck KGaA, Darmstadt, Germany for providing the liquid crystal mixture.

**Competing interests.** The authors declare no competing interests.

## References

1. **ElMossallamy MA, Zhang H, Song L, Seddik KG, Han Z and Li GY** (2020) Reconfigurable intelligent surfaces for wireless communications: Principles, challenges, and opportunities. *IEEE Transactions on Cognitive Communications and Networking* **6**, 990–1002. doi:10.1109/TCCN.2020.2992604
2. **Huang C, Zappone A, Alexandropoulos GC, Debbah M and Yuen C** (2019) Reconfigurable intelligent surfaces for energy efficiency in wireless communication. *IEEE Transactions on Wireless Communications* **18**, 4157–4170. doi:10.1109/TWC.2019.2922609
3. **Gros J-B, Popov V, Odit MA, Lenets V and Lerosey G** (2021) A Reconfigurable Intelligent Surface at mmWave Based on a Binary Phase Tunable Metasurface. *IEEE Open Journal of the Communications Society* **2** 1055–1064. doi:10.1109/OJCOMS.2021.3076271
4. **Pei X, Yin H, Tan L, Cao L, Li Z, Wang K, Zhang K and Björnson E** (2021) RIS-Aided wireless communications: Prototyping, Adaptive beamforming, and indoor/outdoor field trials. *IEEE Transactions on Communications* **69**, 8627–8640. doi:10.1109/TCOMM.2021.3116151
5. **Björnson E, Özdogan O and Larsson EG** (2020) Intelligent reflecting surface versus decode-and-forward: How large surfaces are needed to beat relaying?. *IEEE Wireless Communications Letters* **9**, 244–248. doi:10.1109/LWC.2019.2950624
6. **Jiménez-Sáez A, Asadi A, Neuder R, Delbari M and Jamali V** (2023) Reconfigurable intelligent surfaces with liquid crystal technology: A hardware design and communication perspective.
7. **Jakoby R, Gaebler A and Weickhmann C** (2020) Microwave liquid crystal enabling technology for electronically steerable antennas in satcom and 5g millimeter-wave systems. *Crystals* **10**(514). doi:10.3390/cryst10060514
8. **Perez-Palomino G, Baine P, Dickie R, Bain M, Encinar JA, Cahill R, Barba M and Toso G** (2013) Design and experimental validation of liquid crystal-based reconfigurable reflectarray elements with improved bandwidth in f-band. *IEEE Transactions on Antennas and Propagation* **61**, 1704–1713. doi:10.1109/TAP.2013.2242833
9. **Neuder R, Späth M, Schüßler M and Jiménez-Sáez A** (2024) Architecture for sub-100 ms liquid crystal reconfigurable intelligent surface based on defected delay lines. *Nature Communications Engineering* **3**(70).
10. **Neuder R, Liu Y, Dzieia N, Wang D and Jiménez-Sáez A** (2024) Unit cell design for dual-polarized liquid crystal reconfigurable intelligent surface based on defected delay lines. In *2024 54th European Microwave Conference (EuMC)*. 228–231. doi:10.23919/EuMC61614.2024.10732732
11. **Neuder R, Wang D, Schüßler M, Jakoby R and Jiménez-Sáez A** (2023) Compact liquid crystal-based defective ground structure phase shifter for reconfigurable intelligent surfaces. In *2023 17th European Conference on Antennas and Propagation (EuCAP)*. 1–5. doi:10.23919/EuCAP57121.2023.10133014
12. **Kim S, Chae C-B and Min B-W**. (2023) A low-loss defected-ground-structure based phase shifter and antenna on a 4-$\mu$m thin liquid crystal layer. *IEEE Access* **11**, 34952–34957. doi:10.1109/ACCESS.2023.3264639
13. **Schott** (2018) Electrical Properties of SCHOTT Thin Glasses, Technical Report.
14. **Fritzsch C, Snow B, Sargent J, Klass D, Kaur S and Parri O** (2019) 77-1: Invited paper: Liquid crystals beyond displays: Smart antennas and digital optics. *SID Symposium Digest of Technical Papers* **50**, 1098–1101. doi:10.1002/sdtp.13120
15. **Rose M** 2012. Active Matrix Liquid Crystal Displays (AMLCDs). In J Chen, W Cranton and M Fihn (Eds.) *Handbook of Visual Display Technology*, Springer, Berlin Heidelberg, 1589–1606. doi:10.1007/978-3-540-79567-4_95
16. **Karabey OH, Gaebler A, Strunck S and Jakoby R** (2012) A 2-D electronically steered phased-array antenna with 2 x 2 elements in LC display technology. *IEEE Transactions on Microwave Theory and Techniques* **60**, 1297–1306. doi:10.1109/TMTT.2012.2187919
17. **Delbari M, Neuder R, Jiménez-Sáez A, Asadi A and Jamali V** (2024) Fast transition-aware reconfiguration of liquid crystal-based riss. In *2024 IEEE International Conference on Communications Workshops (ICC Workshops)*. 214–219. doi:10.1109/ICCWorkshops59551.2024.10615422
18. **Díaz-Rubio A and Tretyakov SA** (2021) Macroscopic modeling of anomalously reflecting metasurfaces: Angular response and far-field scattering. *IEEE Transactions on Antennas and Propagation* **69**, 6560–6571.
19. **Diaz-Rubio A, Kosulnikov S and Tretyakov SA** (2022) On the integration of reconfigurable intelligent surfaces in real-world environments: A convenient approach for estimation reflection and transmission. *IEEE Antennas and Propagation Magazine* **64**, 85–95.
20. **Ra'di Y, Sounas DL and Alù A** (2017) Metagratings: Beyond the limits of graded metasurfaces for wave front control. *Physical Review letters* **119**, 067404.
21. **Rostan F and W Wiesbeck** (1995) Design considerations for dual polarized aperture-coupled microstrip patch antennas. *IEEE Antennas and Propagation Society International Symposium. 1995 Digest*. **4**, 2086–2089. doi:10.1109/APS.1995.531005



**Robin Neuder** received the B.S. and M.S. degree in electrical engineering and information technology from TU Darmstadt, Germany in 2019 and 2021, respectively. Since 2021, he has been a Research Assistant with the Institute of Microwave Engineering and Photonics at TU Darmstadt. His research interests include compact liquid-crystal based tuneable planar devices and their integration into Reconfigurable Intelligent Surfaces.



**Ana Díaz-Rubio** was born in Landete, Spain. She received the bachelor's degree in telecommunication engineering and the M.Sc. and Ph.D. degrees from the Polytechnic University of Valencia, Valencia, Spain, in 2010, 2011, and 2015, respectively. She is currently Associate Professor in Universitat Politècnica de València (Spain). Her current research interest includes artificial thin surfaces for controlling wave propagation.



**Yingzhe Liu** is a Radio Frequency R&D Engineer with a background in both theoretical and applied RF technologies. He completed his undergraduate studies at the Universidad Politécnica de Madrid (UPM), graduating from the E.T.S.I.T. (Escuela Técnica Superior de Ingenieros de Telecomunicación) with a focus on RF systems. He further pursued his Master's degree at the Technische Universität Darmstadt, Germany, specializing in the RF Technology. Currently, Yingzhe is part of the engineering team at TRUMPF, where he is engaged in the development of critical 13.56 MHz RF generator. These systems are essential components for semiconductor fabrication equipment, such as plasma etching and deposition tools, which are fundamental to the microchip manufacturing industry. His work effectively bridges academic research with high-impact industrial applications in the semiconductor sector.



**Nora Dzieia** received the B.Sc. degree in electrical engineering from TU Darmstadt and continued her education afterwards at Chalmers University of Technology in Gothenburg, Sweden. For her M.Sc. she is studying wireless, photonic and space engineering and focuses mainly on integrated photonics.



**Dongwei Wang** was born in Taiyuan, Shanxi, China. He received the B.Eng. degree from Zhejiang University, Hangzhou, Zhejiang, China, in 2014, and the M.Sc. degree from the Karlsruher Institut für Technologie, Karlsruhe, Germany, in 2018. He received Dr. Ing. degree in electrical engineering from Technische Universität Darmstadt, Darmstadt, Germany, in 2023. Since then, he joined Bosch Corporate Research Renningen, Germany. His research interests include electronically reconfigurable RF system and components, RF materials and automotive radar hardware.



**Alejandro Jiménez-Sáez** (S'15, M'22) received the master's degrees (Hons.) in telecommunications engineering from the Polytechnic University of Valencia, Spain, and in electrical engineering from the Technical University of Darmstadt, Germany, in 2017. In 2021, he received the Dr.-Ing. degree (with distinction) in electrical engineering from the TU Darmstadt and the Freunde der TU Darmstadt prize for the best dissertation in electrical engineering. He obtained the Athene Young Investigator award at TU Darmstadt and leads the Smart RF Systems based on Artificial and Functional Materials independent research group. His current research interests include chipless RFID, electromagnetic bandgap structures, liquid crystal, and reconfigurable intelligent surfaces.

https://doi.org/10.1017/S1759078725102596 Published online by Cambridge University Press